J. Fluid Mech. (2006), vol. 547, pp. 297–316. © 2006 Cambridge University Press
doi:10.1017/S0022112005007305 Printed in the United Kingdom

A comparison of blob methods for vortex sheet roll-up

By GREGORY R. BAKER[1] AND LAN D. PHAM[2]

[1]Ohio State University, Columbus, Ohio, USA

[2]University of California, Irvine, California, USA

(Received 12 October 2004 and in revised form 15 June 2005)

The motion of vortex sheets is susceptible to the onset of the Kelvin–Helmholz instability. There is now a large body of evidence that the instability leads to the formation of a curvature singularity in finite time. Vortex blob methods provide a regularization for the motion of vortex sheets. Instead of forming a curvature singularity in finite time, the curves generated by vortex blob methods form spirals. Theory states that these spirals will converge to a classical weak solution of the Euler equations as the blob size vanishes. This theory assumes that the blob method is the result of a convolution of the sheet velocity with an appropriate choice of a smoothing function. We consider four different blob methods, two resulting from appropriate choices of smoothing functions and two not. Numerical results indicate that the curves generated by these methods form different spirals, but all approach the same weak limit as the blob size vanishes. By scaling distances and time appropriately with blob size, the family of spirals generated by different blob sizes collapse almost perfectly to a single spiral. This observation is the next step in developing an asymptotic theory to describe the nature of the weak solution in detail.

1. Introduction

Originally, vortex sheets were viewed as models for thin shear layers based on physical intuition. This view has been verified formally by Moore (1978), Baker & Shelley (1990) and Dhanak (1994*a*, *b*) who show that a vortex sheet is the limit as the thickness of a shear layer vanishes. The assumptions underlying this work are those normally associated with a long wave limit, so, perhaps, it is not too surprising that vortex sheet motion suffers from the spontaneous appearance of singularities as often happens in long wave models. See Cowley, Baker & Tanveer (1999) for both a review and a consistent asymptotic theory that supports the evidence for the formation of a curvature singularity on a vortex sheet in finite time t_s. Caflisch & Orellana (1989) establish that singular solutions are closely associated with the ill-posedness of vortex sheet motion. Results from standard applications of numerical techniques to vortex sheet motion have been bedevilled by the onset of irregular motion of the points representing the sheet, driven by the ill-posed nature of vortex sheet motion. Hopes that vortex sheets could be used reliably as models for thin shear flows, such as wakes shed by bodies, were damped, if not dashed.

The introduction of vortex blob methods by Chorin & Bernard (1973) and Kuwahara & Takami (1973) opened up new directions for the study of vortex sheet motion. The points representing the vortex sheet are replaced by vortices of prescribed (and fixed) shape. Numerical calculations show regular motion for the centres of the blobs even after t_s and, moreover, the motion shows the formation of a spiral, the expected physical behaviour. In particular, Krasny (1986*b*) uses a special form of the vortex blob method to calculate the roll-up of a periodic vortex sheet which results from the classical Kelvin–Helmholtz instability. However, details of the spiral structure depend on the choice of the size of the vortex blob, measured by a parameter δ. Further, there is no direct link between the choice of δ and some physical regularization such as the thickness of the shear layer or the presence of viscosity. Comparisons with direct numerical simulations of the viscous motion by Tryggvason, Dahm & Sbeih (1991) and inviscid layers of small thickness by Baker & Shelley (1990) show good agreement away from the spiral centre.

Liu & Xin (1995) have placed the use of blob methods for vortex sheet motion on a sound footing by proving that in the limit of $\delta \to 0$ the vortex sheet approaches a classical weak solution to the Euler equations. The existence of a weak solution when the vortex sheet strength is of one sign has been established by Delort (1991) and Majda (1993). Of course, the weak solution is unlikely to be unique and will depend on the choice of regularization. The proof of Liu & Xin (1995) uses several assumptions, the one of interest here is that the blob method is the result of a convolution with a suitably defined smoothing function. For example, Krasny (1987) uses an appropriate smoothing function, which has an algebraic decay, to study roll-up of trailing vortices in the wake of an aircraft. Curiously, Krasny (1986*b*) does not use the periodic version of this blob method, but introduces a modified version that has a simple form for periodic motion. The underlying smoothing function is not identified. We derive the smoothing function in this article, and show that it does not satisfy the sufficient conditions of Liu & Xin (1995) for convergence to a weak solution. Nevertheless, numerical results still show apparent convergence as $\delta \to 0$. Perhaps the sufficient conditions of Lui & Xin (1995) are not necessary.

Beale & Majda (1985) suggest a family of blob methods based on the choice of a Gaussian profile for the smoothing function multiplied by a specific polynomial whose order dictates the degree of accuracy in the approximation. The leading member of this family satisfies the assumptions of the theory of Liu & Xin (1995), and thus provides a different blob method which will converge to a weak solution. The interest here, then, is whether different blob methods give different weak solutions.

We consider four different blob methods: two of them are convolutions with an appropriate smoothing function, and two are regularizations without a clear connection to a convolution with an appropriate smoothing function. Numerical results indicate that the curves form spirals that are different, but approach the same weak limit as $\delta \to 0$ for all four cases. For times before t_s, the curves calculated with different δ approach the vortex sheet linearly in δ. After t_s, the situation is different. For points on the curves away from the spiral region, the convergence is linear, but in the spiral region the convergence is different.

Animations of the motion of the spirals suggest they rotate uniformly, and by tracking the angle of the tangent at the spiral centre we observe a linear growth in time with the rate of growth dependent on δ. By picking a specific angle θ, we may compare spirals determined with different values of δ geometrically. Of course, the time T it takes the tangent at the spiral centre to reach θ depends on δ: the numerical results indicate this dependency is linear for small enough δ. Consequently, by an appropriate scaling in time we may coordinate all spirals with different δ to have the same angle for the tangents at their centres. By a further rescaling of distances by δ, the spirals collapse almost perfectly onto one spiral. The results suggest that the spiral may be expressed in a simple form, at least in the limit of vanishing δ, and this form must satisfy a specific version of the vortex sheet equation of motion. However, challenges remain on how to connect the solution to the motion of the vortex sheet outside the spiral.

2. Mathematical preliminaries

For a comprehensive, detailed treatment of vorticity and the streamfunction, see Majda & Bertozzi (2002). Here, we simply provide an overview with an emphasis on the origin of blob methods.

The velocity $\boldsymbol{u} = (u, v)$ generated by a vorticity distribution ω in two-dimensional flow can be given in terms of derivatives of the streamfunction ψ where

$$\psi(x, y) = -\int_{-\infty}^{\infty}\int_{-\infty}^{\infty} \omega(x', y')\, G(x - x', y - y')\, \mathrm{d}x'\, \mathrm{d}y'. \tag{2.1a}$$

Here, G is the free-space Green function for Laplace's equation:

$$G(x, y) = \frac{1}{4\pi} \ln(x^2 + y^2). \tag{2.1b}$$

These results are valid even when the vorticity is singular, for example, when the vorticity corresponds to a vortex sheet, the case of interest in this study. Then, $\omega = \gamma(s)\, \delta(n)$ where n is the normal to the sheet and s the arclength along it from some reference point.

Vortex sheets form curvature singularities in finite time where derivatives of the velocity become singular. One way to avoid the formation of singularities is to convolute the ψ with a cutoff function ϕ_δ that ensures smooth velocities as a consequence and so regularizes the motion of the sheet. Let

$$\psi_\delta(x, y) = \int_{-\infty}^{\infty}\int_{-\infty}^{\infty} \psi(x - x', y - y')\, \phi_\delta(x', y')\, \mathrm{d}x'\, \mathrm{d}y' \tag{2.2a}$$

be the smoothed streamfunction. By substituting (2.1a) into (2.2a), we may express the smoothed streamfunction in terms of the vorticity and a smoothed Green function G_δ:

$$\psi_\delta(x, y) = \int_{-\infty}^{\infty}\int_{-\infty}^{\infty} \omega(x', y')\, G_\delta(x - x', y - y')\, \mathrm{d}x'\, \mathrm{d}y', \tag{2.2b}$$

$$G_\delta(x, y) = \int_{-\infty}^{\infty}\int_{-\infty}^{\infty} G(x - x', y - y')\phi_\delta(x', y')\, \mathrm{d}x'\, \mathrm{d}y'. \tag{2.2c}$$

While many choices of ϕ_δ will regularize the motion of the curve, the desirable choices are those that ensure that the curve approaches a weak solution to Euler's equations as $\delta \to 0$. According to Lui & Xin (1995), the choice $\phi_\delta(x, y) = \phi(x/\delta, y/\delta)/\delta^2$ will ensure convergence to a weak limit if $\phi(x, y)$ satisfies the following conditions:

(i) $\phi > 0$ has continuous second-order derivatives and decays at least as fast as $1/|\boldsymbol{x}|^3$,

(ii)

$$\int_{-\infty}^{\infty}\int_{-\infty}^{\infty} \phi(x, y)\, \mathrm{d}x\, \mathrm{d}y = 1, \tag{2.3a}$$

(iii)

$$\iint\limits_{|\mathbf{x}|<1} \phi(x, y)\,\mathrm{d}x\,\mathrm{d}y \geqslant \tfrac{1}{2}. \tag{2.3b}$$

Krasny's (1987) choice

$$G_\delta(x, y) = \frac{1}{4\pi}\ln(x^2 + y^2 + \delta^2), \tag{2.4a}$$

which arises from the smoothing function

$$\phi_\delta(x, y) = \frac{1}{\pi}\left(\frac{\delta}{x^2 + y^2 + \delta^2}\right)^2, \tag{2.4b}$$

is a good example that satisfies the conditions to ensure convergence to a weak limit. Another choice is that of Beale & Majda (1985)

$$G_\delta(x, y) = \frac{1}{4\pi}\int_0^{x^2+y^2} \frac{1 - \exp(-r/\delta^2)}{r}\,\mathrm{d}r, \tag{2.5a}$$

which arises from the smoothing function

$$\phi_\delta(x, y) = \frac{1}{\pi\delta^2}\exp\left(-\frac{(x^2 + y^2)}{\delta^2}\right). \tag{2.5b}$$

2.1. *Periodic blobs*

Now let us turn our attention to velocities that are 2π-periodic in x. Obviously, the vorticity ω will also be 2π-periodic. With the additional restriction that v has no mean value, the streamfunction ψ will also be 2π-periodic which may be expressed in terms of a periodic Green function;

$$\psi(x, y) = \int_{-\infty}^{\infty}\int_0^{2\pi} \omega(x', y')\,G_p(x - x', y - y')\,\mathrm{d}x'\,\mathrm{d}y', \tag{2.6a}$$

where

$$G_p(x, y) = \sum_{k=-\infty}^{\infty} G(x + 2k\pi, y) = \frac{1}{4\pi}\ln\left(\cosh(y) - \cos(x)\right). \tag{2.6b}$$

is calculated by the method of images (for details, see Saffman 1992, §7.4).

If we convolute a periodic streamfunction ψ with a cutoff function ϕ_δ, we obtain a periodic smoothed streamfunction ψ_δ from (2.2*a*). When we substitute (2.6*a*) into (2.2*a*), we must replace (2.2*b*) and (2.2*c*) with

$$\psi_\delta(x, y) = \int_{-\infty}^{\infty}\int_0^{2\pi} \omega(x', y')\,G_{p\delta}(x - x', y - y')\,\mathrm{d}x'\,\mathrm{d}y', \tag{2.7a}$$

$$G_{p\delta}(x, y) = \int_{-\infty}^{\infty}\int_0^{2\pi} G_p(x - x', y - y')\phi_\delta(x', y')\,\mathrm{d}x'\,\mathrm{d}y'. \tag{2.7b}$$

Now let us consider the periodic extension of Krasny's smoothing function (2.6*b*). By the method of images, we find

$$G_{p\delta} = \frac{1}{4\pi}\ln(\cosh\sqrt{y^2 + \delta^2} - \cos(x)), \tag{2.8a}$$

which corresponds to the periodic smoothing function

$$\phi_{p\delta} = \frac{1}{4\pi}\frac{\delta^2}{(y^2+\delta^2)^{3/2}}\left\{\frac{\sqrt{y^2+\delta^2}\,[\cos(x)\cosh\sqrt{y^2+\delta^2}-1]}{[\cosh\sqrt{y^2+\delta^2}-\cos(x)]^2}\right.$$
$$\left.+\frac{\sinh\sqrt{y^2+\delta^2}\,[\cosh\sqrt{y^2+\delta^2}-\cos(x)]}{[\cosh\sqrt{y^2+\delta^2}-\cos(x)]}\right\}. \qquad (2.8b)$$

While the form of $G_{p\delta}$ looks simple, it results in somewhat complicated expressions for the velocities. Krasny (1986*b*) introduces instead the much simpler form,

$$G_{p\delta} = -\frac{1}{4\pi}\ \ln(\cosh y - \cos(x) + \delta^2), \qquad (2.9a)$$

which corresponds to the periodic smoothing function

$$\phi_{p\delta} = \frac{\delta^2}{4\pi}\frac{\cosh(y)+\cos(x)}{(\cosh(y)-\cos(x)+\delta^2)^2}. \qquad (2.9b)$$

The underlying smoothing function that generates this periodic version is derived in the Appendix:

$$\phi_\delta = \frac{\delta^2}{\pi}\left[\frac{\alpha(L^2-x^2)}{(L^2+x^2)^2}+\frac{\beta L}{L^2+x^2}\right], \qquad (2.9c)$$

where

$$\alpha = \frac{\cosh(y)+\cosh(L)}{2\sinh^2(L)}, \qquad (2.9d)$$

$$\beta = \frac{1+\cosh(y)\cosh(L)}{2\sinh^3(L)}, \qquad (2.9e)$$

and

$$\exp(-L) = \cosh(y) + \delta^2 - \sqrt{(\cosh(y)+\delta^2)^2-1}. \qquad (2.9f)$$

For small values of x, y and δ, (2.9*c*) takes the form of (2.4*b*), but the far-field behaviour is very different:

$$\phi_\delta \approx \frac{\delta^2}{\pi}\,\mathrm{e}^{-|y|}\,\frac{|y|(x^2+y^2)+2(y^2-x^2)}{(x^2+y^2)^2}. \qquad (2.10)$$

The form of (2.9*c*) does not satisfy the property $\phi_\delta = \phi(x/\delta, y/\delta)/\delta^2$. There is no current theoretical guarantee that this choice will converge to a weak limit. We will provide numerical evidence that the results from using (2.8*a*) and (2.9*a*) are very similiar, and it is therefore likely that the sufficient conditions of Lui & Xin (1995) are not necessary for convergence to a weak limit.

We are unaware of any closed forms for the sums of (2.7). Fortunately, the sums can be evaluated accurately by keeping only the terms $k = -1, 0, 1$ because of the rapid decay of the Gaussians for large arguments.

2.2. *Vortex sheet motion*

A vortex sheet is a singular distribution of vorticity along a curve. Specifically, $\omega = \gamma(p)\,\delta(n)$ where n is the normal to the sheet and p is a Lagrangian label for a marker on the sheet given in parametric form $\boldsymbol{x}(p,t) = (x(p,t), y(p,t))$. The motion of this marker may be obtained by differentiating (2.1*a*) and setting its velocity to be that of the average velocity determined by taking the principal value of the resulting contour integral. Details are available in Saffman (1992) or Majda & Bertozzi (2002). As a consequence of these steps,

$$\frac{\partial \boldsymbol{x}}{\partial t}(p,t) = \int_{-\infty}^{\infty} \gamma(p')\, \boldsymbol{K}(\boldsymbol{x}(p,t), \boldsymbol{x}(p',t))\, \mathrm{d}p', \tag{2.11a}$$

where

$$\boldsymbol{K}(\boldsymbol{x},\boldsymbol{x}') = \left(-\frac{\partial G}{\partial y}(x-x', y-y'), \frac{\partial G}{\partial x}(x-x', y-y') \right). \tag{2.11b}$$

For 2π-periodic vortex sheet motion, we have $x(p+2\pi) = 2\pi + x(p)$, $y(p+2\pi) = y(p)$ and $\gamma(p+2\pi) = \gamma(p)$. We may replace the range of integration in (2.11*a*) by a 2π interval, and use the periodic version of G (2.6*b*) in (2.11*b*) which gives

$$\boldsymbol{K}(\boldsymbol{x},\boldsymbol{x}') = \frac{1}{4\pi} \frac{(-\sinh(y-y'),\ \sin(x-x'))}{\cosh(y-y') - \cos(x-x')}. \tag{2.12}$$

Vortex blob methods are a consequence of replacing G by G_δ. We make four choices. First, we use (2.8*a*) to obtain

$$\boldsymbol{K}_{BP}(\boldsymbol{x},\boldsymbol{x}') = \left(-\frac{(y-y')}{\sqrt{(y-y')^2+\delta^2}} \sinh \sqrt{(y-y')^2+\delta^2}, \sin(x-x') \right) \Big/ D, \tag{2.13a}$$

where

$$D = 4\pi[\cosh(\sqrt{(y-y')^2+\delta^2}) - \cos(x-x')]. \tag{2.13b}$$

This form is rather cumbersome and expensive to evaluate, but it conforms to the assumptions used by Lui & Xin (1995) to prove convergence of the vortex blob method and the existence of a weak limit.

Secondly, we use Krasny's choice (2.9*a*) which leads to

$$\boldsymbol{K}_K(\boldsymbol{x},\boldsymbol{x}') = \frac{1}{4\pi} \frac{(-\sinh(y-y'),\ \sin(x-x'))}{\cosh(y-y') - \cos(x-x') + \delta^2}. \tag{2.14}$$

The other two smoothed kernels come from the periodic version of the first member of the Beale & Majda family (1985). By using (2.5*a*) with the method of images,

$$\begin{aligned}\boldsymbol{K}_{BM}(\boldsymbol{x},\boldsymbol{x}') = \frac{1}{4\pi} \frac{(-\sinh(y-y'), \sin(x-x'))}{\cosh(y-y') - \cos(x-x')} - 2\sum_{k=-\infty}^{\infty} \frac{(-(y-y'), (x-x'+2\pi k))}{(x-x'+2\pi k)^2 + (y-y')^2} \\ \times \exp[-((x-x'+2\pi k)^2 + (y-y')^2)/\delta^2].\end{aligned} \tag{2.15}$$

Because of the rapid decay of the Gaussian for large arguments, only three terms in the sum, $k = -1, 0, 1$, are required for an accurate evaluation of the sums. The obvious way to avoid the sums is to incorporate Krasny's idea expressed in (2.14) into the kernel (Beale, personal communication)

$$\begin{aligned}\boldsymbol{K}_{BMK}(\boldsymbol{x},\boldsymbol{x}') = \frac{1}{4\pi} \frac{(-\sinh(y-y'),\ \sin(x-x'))}{\cosh(y-y') - \cos(x-x')} \\ \times \{1 - \exp[-2(\cosh(y-y') - \cos(x-x'))\delta^2]\}.\end{aligned} \tag{2.16}$$

Notice that a factor of two has been inserted into the argument of the Gaussian. This factor of two ensures that the Gaussians in (2.15) and (2.16) approach the same form as p' aprroaches p. Unfortunately, we do not know whether the kernel (2.16) results from the convolution with a smooth cutoff function that satisfies the assumptions in the theory of Liu & Xin (1995). On the other hand, (2.15) does.

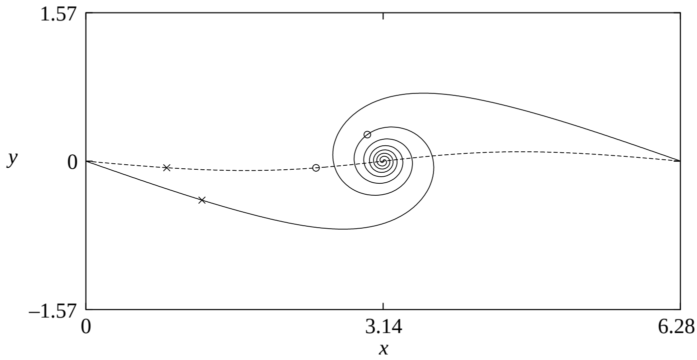

FIGURE 1. The position of the sheet at two times: $t = 1.005$ (dashed) and $t = 6.283$ (solid). Also shown are the locations of the Lagrangian points $p = \pi/4$ ($\times$) and $p = 3\pi/4$ ($\circ$).

3. Numerical results

All four choices of the vortex blob methods described in the previous section are used to calculate the roll-up of a spiral that forms as a consequence of Kelvin–Helmholtz instability. The first objective is to compare the spirals and determine whether they approach the same weak limit as $\delta \to 0$. Subsequently, we seek to determine the dependency of the structure of the spirals on δ. It is the precise nature of the scalings of the structure with δ that is required to form an asymptotic theory that will describe the nature of the weak solution as $\delta \to \infty$.

3.1. *Numerical implementation*

There are two numerical tasks to perform in calculating the evolution of a vortex sheet using (2.11*a*) with smoothed kernels. The first is to calculate the integral numerically. This is done using the spectrally accurate trapezoidal rule introduced by Baker (1983) and analysed subsequently by Sidi & Israeli (1988). The second task is to evolve the vortex sheet position in time. The fourth-order Runge–Kutta method can be used to obtain the position for the first four time steps. For all others, the fourth-order Adams–Bashford method is used. More details are available in Pham (2001).

We use Krasny's (1986*b*) initial condition which is a small perturbation of a flat vortex sheet by the sinusoidal perturbation that grows unstably.

$$x(p, 0) = p + \frac{2\pi}{100} \sin p\,, \quad y(p, 0) = -\frac{2\pi}{100} \sin p. \tag{3.1}$$

The factors of 2π are present because Krasny uses a periodicity of 1 whereas we use a periodicity of 2π. Otherwise, (3.1) is exactly the same as Krasny's (1986*b*) choice. We run our code up to a final time $T = 2\pi$ which is well past the singularity time t_s, estimated by Krasny (1986*a*) to be $3/8 \times (2\pi)$, where the vortex sheet develops a curvature singularity without the δ regularization. Typical vortex sheet locations are shown in figure 1 at two different times, $t = 0.16 \times (2\pi) = 1.005$ which is before the singularity time, and $t = 2\pi = 6.283$ which is well past the singularity time. Although the vortex sheet locations are shown for the specific choice $\delta = 0.1$, the results are typical in that the sheet evolves slowly at first then rapidly forms a spiral which spins around creating more and more arms. The questions we explore here concern the comparisons of the spirals generated by different δ-regularizations, and the nature of the spiral as $\delta \to 0$. In the former regard, we show also the locations of two

δ	N	$\Delta t/(2\pi)$	E_s	E_t	$t_{restart}$
0.1	1024	0.00125	1.5×10^{-6}	1.4×10^{-5}	
0.09	1024	0.00125	1.4×10^{-5}	3.1×10^{-5}	
0.08	1024	0.00125	8.9×10^{-5}	7.2×10^{-5}	
0.07	2048	0.000625	3.2×10^{-6}	6.6×10^{-6}	
0.06	2048	0.000625	6.4×10^{-5}	2.0×10^{-5}	
0.05	4096	0.000625	3.9×10^{-5}	7.4×10^{-5}	
0.04	2048	0.0003125	3.9×10^{-13}	4.5×10^{-12}	2.199
	4096	0.0003125	2.9×10^{-4}	2.0×10^{-5}	
0.03	4096	0.00015625	1.7×10^{-9}	7.8×10^{-9}	2.953
	8192	0.00015625	1.2×10^{-4}	2.3×10^{-6}	

TABLE 1. Measuring the spatial error E_s and temporal error E_t as a function of N and Δt.

Lagrangian points defined by $p = \pi/4$ and $p = 3\pi/4$. These points will be used later to assess the convergence in δ.

The accuracy of the vortex sheet location is controlled in the following way. Let the smoothing parameter δ be fixed. Let $\boldsymbol{x}_{i,k}$ be the marker locations for the vortex sheet at $t = k\Delta t$ using N points. Similarly, let $\boldsymbol{x}^{(s)}_{i,k}$ and $\boldsymbol{x}^{(t)}_{i,k}$ be the locations when $2N$ points are used and when a time step $0.5\Delta t$ is used. An estimate for the spatial error is obtained by seeking $E_s = \max|\boldsymbol{x} - \boldsymbol{x}^{(s)}|$ where the maximum is taken over all common spatial points and time levels. Similarly, the temporal error is $E_t = \max|\boldsymbol{x} - \boldsymbol{x}^{(t)}|$. Table 1 shows the required resolution to achieve the errors shown for $\boldsymbol{K}_{BP}$.

It is clear that as $\delta \to 0$, it becomes increasingly more difficult to obta good accuracy. We introduce two important modifications to help achieve high accurcacy. First, we note that the accuracy deteriorates rapidly for times beyond the formation of a spiral. Thus, we split the calculations into subintervals of time and increase the resolution as required for later times. For example, we ran our code for $\delta = 0.4$ up to $t = 2.199$ with 2048 points and a time step of $0.0003125 \times 2\pi$ with exceptional accuracy. After that time the accuracy deteriorates significantly. We restart the calculation at $t = 2.199$ with more points by simply using interpolation based on a Fourier series. In this way, we achieve the accuracy shown in table 1. This strategy is repeated for the smaller choices of δ.

Secondly, we find that round-off errors become increasingly significant as δ is reduced. While the inclusion of δ regularizes the integrand of the Biot-Savart integral, the integrand suffers catastrophic cancellation for contributions on either side of $p' = p$ (see (2.13*a*)). The remedy is to subtract a suitable multiple of the integral

$$\int_0^{2\pi} [\sin(x(p) - x(p'))x_p(p') + F(p, p')(y(p) - y(p'))y_p(p')] \frac{\mathrm{d}p'}{D(p, p')}, \tag{3.2}$$

where

$$F(p, p') = \frac{\sinh\sqrt{(y(p) - y(p'))^2 + \delta^2}}{\sqrt{(y(p) - y(p'))^2 + \delta^2}},$$

and D is given in (2.13*b*). The integrand now remains of one sign and has a double root at $p' = p$. Further, the integrand does not become large for small δ.

Lastly, application of the Krasny spectral filter prevents any growth of round-off errors: the filter level is set at 10^{-15}.

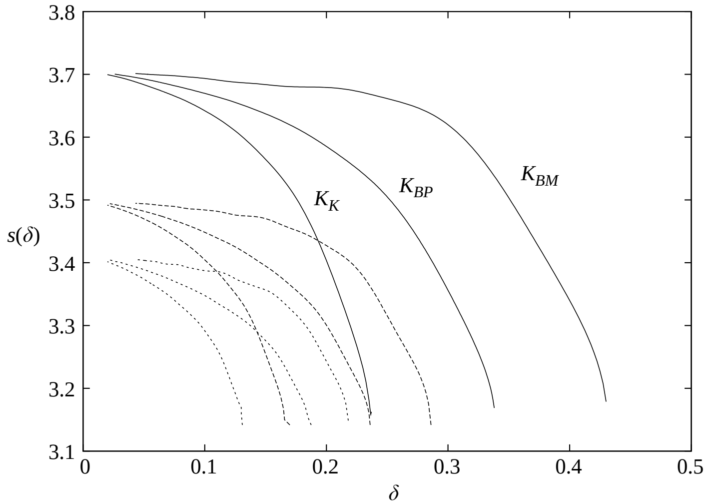

FIGURE 2. The location of the first three outer arms $s(\delta)$ for three methods as δ is varied. —, first; - - -, second; . . . , third.

3.2. *Convergence to a weak limit*

All four smoothed kernels show the formation of a spiral after t_s, centred at the point $(\pi, 0)$. The spirals are similar, but differ in detail. The first task, then, is to establish whether these spirals tend to the same spiral as $\delta \to 0$. We follow Krasny (1986*b*) in choosing the locations where the spiral arms cross the x-axis as a measure of the spirals. Specifically, we seek the intersection locations $x = s_j(\delta)$ along the segment $(\pi, 2\pi) \times \{0\}$. The set $S(\delta)$ with $m(\delta)$ elements can be ordered from large to small

$$s_1(\delta) > s_2(\delta) > \ldots > s_{m(\delta)}(\delta).$$

With decreasing δ, the spiral has more and more spiral arms. Thus, the number of intersection points $m(\delta)$ is an increasing function with decreasing δ. The objective, then, is to study

$$\lim_{\delta \to 0} s_j(\delta),$$

and to assess whether the limit is the same for all the kernels.

The numerical data consists of the set $\{\,(x_j, y_j) : 0 \leqslant j \leqslant N\,\}$ where $x_j = x(j\Delta p)$, $y_j = y(j\Delta p)$ and $\Delta p = 2\pi/N$. The functions $x(p) - p$ and $y(p)$ are both odd functions of p. Smooth functions $\tilde{x}(p) - p$ and $\tilde{y}(p)$ can be constructed as a sum of sines with the coefficients given by the discrete Fourier transform. Then, the intersection point $s_i(\delta)$ can be determined by finding the roots of $\tilde{y}(p)$. This task is carried out numerically by Newton's method once the interval in which y_j changes sign has been located. The first guess for Newton's method is the midpoint of the interval.

In figure 2, we plot the first three outer arms, $s_1(\delta)$, $s_2(\delta)$ and $s_3(\delta)$, at $t = 2\pi$ for three of the kernels. Results for the kernel $\boldsymbol{K}_{MBK}$ are not shown simply because they are barely discernible from the results using $\boldsymbol{K}_{BM}$. The order in the location of the arms remains consistent for the three choices shown, so we have indicated which kernel produces each curve only for the first arm.

The results suggest strongly that the outer arms all tend to the same limit as $\delta \to 0$, but at different rates. The rates clearly depend on the form of the cutoff function. For the two kernels associated with the Gaussian smoothing function the rates are very close. The reason is that the forms are similar as p' approaches p: the insertion of a factor 2 in the argument of the exponential of $\boldsymbol{K}_{BMK}$ (2.16) guarantees this since

$$2\frac{\cosh(y-y')-\cos(x-x')}{\delta^2} \approx \frac{(x-x')^2+(y-y')^2}{\delta^2}, \tag{3.3a}$$

when x', y' are close to x, y.

Similarly, we may compare the expansions of the denominators of the smoothed kernels $\boldsymbol{K}_{BP}$ and $\boldsymbol{K}_K$. From (2.13b) and (2.14),

$$[\cosh(\sqrt{(y-y')^2+\delta^2})-\cos(x-x')] \approx \frac{(x-x')^2+(y-y')^2+\delta^2}{2}, \tag{3.3b}$$

$$\cosh(y-y')-\cos(x-x')+\delta^2 \approx \frac{(x-x')^2+(y-y')^2+2\delta^2}{2}. \tag{3.3c}$$

The forms match if the δ in $\boldsymbol{K}_K$ is replaced by $\sqrt{2}\,\delta$. When δ is rescaled, the curve for $\boldsymbol{K}_{\mathrm{K}}$ falls very close to that of $\boldsymbol{K}_{BP}$. Unfortunately, there is no obvious way to connect the δ terms in $\boldsymbol{K}_{BP}$ and $\boldsymbol{K}_{BM}$.

The results also illustrate that the spirals for the Gaussian kernels are much more tightly wound for the same choice of δ. For example, when $\delta = 0.2$, $\boldsymbol{K}_K$ produces one arm of the spiral; $\boldsymbol{K}_{BP}$ produces two arms; while $\boldsymbol{K}_{BM}$ or $\boldsymbol{K}_{BMK}$ produce at least three arms. Presumably, the short-range influence of the Gaussian smoothing functions, in contrast to the long-range influence of the algebraic decay in the other smoothing functions, produces the more tightly wound spirals.

Fits of the data to a straight line for small δ support the visual impression that the location of the arms approach the same limit. For $\boldsymbol{K}_K$, data in the range $0 < \delta < 0.03$ produces the straight line fits;

$$\begin{aligned} s_1 &= -0.4315\delta + 3.708, \\ s_2 &= -0.6061\delta + 3.504, \\ s_3 &= -0.7935\delta + 3.418. \end{aligned}$$

For $\boldsymbol{K}_{BP}$ and data in the range $0 < \delta < 0.05$, we obtain

$$\begin{aligned} s_1 &= -0.3147\delta + 3.709, \\ s_2 &= -0.4380\delta + 3.504, \\ s_3 &= -0.5535\delta + 3.417. \end{aligned}$$

Finally, for $\boldsymbol{K}_{BM}$ and $0 < \delta < 0.1$,

$$\begin{aligned} s_1 &= -0.1262\delta + 3.707, \\ s_2 &= -0.1978\delta + 3.504, \\ s_3 &= -0.3032\delta + 3.419. \end{aligned}$$

The intercepts of the straight lines for the location of each arm show remarkable agreement for all the kernels. However, the data do not fall perfectly on the straight lines. Instead, there is a noticable oscillation in the data about each straight line with the oscillations decreasing as δ decreases. It is only the averaged trend that supports the fit to straight lines with common intercepts. These oscillations in the location of the arms can be most clearly seen for $\boldsymbol{K}_{BM}$ in figure 2. By watching animations of the motion of the spirals the explanation becomes clear. As the spiral centre turns and creates a new arm, the remaining arms pulse outwards by a small

δ	$p = \pi/4$ x	y	$p = 3\pi/4$ x	y
0.10	0.8540464	−0.0693656	2.430926	−0.0709793
0.09	0.8541808	−0.0696088	2.431211	−0.0713376
0.08	0.8543159	−0.0698536	2.431500	−0.0717026
0.07	0.8544515	−0.0701002	2.431796	−0.0720746
0.06	0.8545877	−0.0703484	2.432097	−0.0724537
0.05	0.8547244	−0.0705983	2.432403	−0.0728402
0.04	0.8548617	−0.0784975	2.432716	−0.0732343
0.03	0.8549995	−0.0711029	2.433035	−0.0736364
0.02	0.8551378	−0.0713575	2.433361	−0.0740466
0.01	0.8552766	−0.0716138	2.433694	−0.0744651
0.00	0.8554159	−0.0718716	2.434033	−0.0748924

TABLE 2. Location of the Lagrangian markers as δ is varied.

amount along a radial ray. The larger deviation occurs on the spiral arms nearest the centre. Overall, the appearance is that of a travelling wave synchronized on all the arms and rotating uniformly around the spiral centre. An important consequence of this wave is that its presence for the choice of kernels $\boldsymbol{K}_K$ and $\boldsymbol{K}_{BP}$, while not easily noticeable, is sufficient to affect any attempt at a higher-order polynomial fit to the location of the arms. Later, we will demonstrate the data matches to a special form. In the meantime, we will confirm that before the singularity time or outside of the spiral region, the sheet does converge linearly in δ.

To that end, consider the locations of the Lagrangian markers $p = \pi/4$ and $p = 3\pi/4$ shown in figure 1. In table 2, we give the locations of the markers as δ is decreased at a time $t = 0.16 \times (2\pi) = 1.005$ before t_s. We include the location when $\delta = 0.0$, which must be computed in a special way to avoid the rapid growth of round-off errors as pointed out by Krasny (1986*a*). He introduced a spectral filter that sets to zero all amplitudes in the Fourier spectrum that fall below a certain level. We also use that filter with $N = 512$ points and a time step of $0.000625 \times (2\pi)$.

The data in table 2 for $\delta \neq 0$ falls almost perfectly on straight lines:

$$x(\pi/4) = 0.8554 - 0.0137\delta, \tag{3.4a}$$

$$y(\pi/4) = -0.0718 + 0.0250\delta, \tag{3.4b}$$

$$x(3\pi/4) = 2.4340 - 0.0307\delta, \tag{3.4c}$$

$$y(3\pi/4) = -0.0748 + 0.0387\delta. \tag{3.4d}$$

Moreover, their intercepts agree very closely to the values calculated with $\delta = 0$.

For the later time $t = 2\pi = 6.283$, we have no sheet location for $\delta = 0$, but we may still determine whether the coordinates fall on straight lines in δ. This is true for the Lagrangian marker at $p = \pi/4$, but is not true for the one at $p = 3\pi/4$. In figure 3, we show the variation of the x-coordinate of the markers $p = \pi/4$ and $p = 3\pi/4$ with δ. A straight line fit of the data for $p = \pi/4$ shows that it falls very close to a straight line, whereas the data for $p = 3\pi/4$ is not close to a straight line at all.

Our results show that even beyond the singularity formation time, regions of the sheet well away from the spiral still converge linearly in δ. On the other hand, the behaviour for markers inside the spiral region is different. The way forward is to note that the centre of the spiral appears to be in solid-body rotation. To confirm this

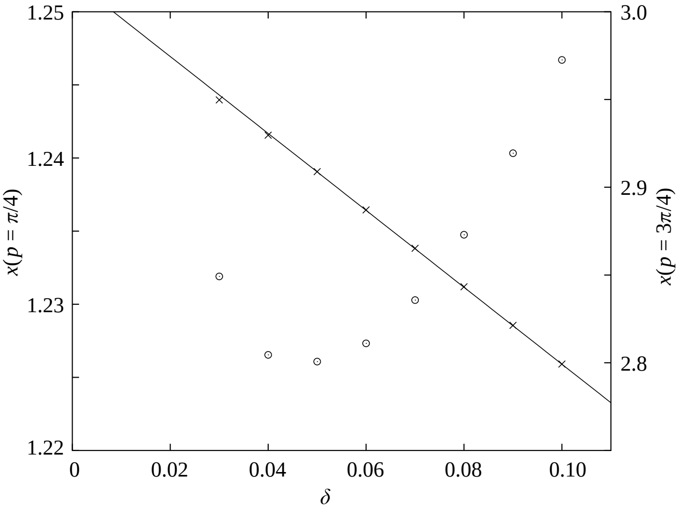

FIGURE 3. Variation of the x-coordinates with δ for the two markers $p = \pi/4$ ($\times$) and $p = 3\pi/4$ ($\bigcirc$). Also shown is the straight line fit to the data for $p = \pi/4$.

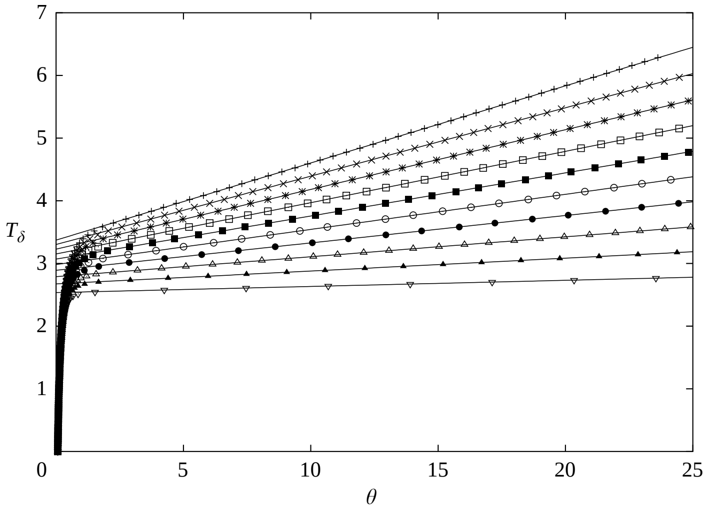

FIGURE 4. Time as a function of the sheet angle at the centre for δ ranging from 0.01 to 0.10 in steps of $\Delta\delta = 0.1$; $\delta = 0.1$ (+), $\delta = 0.01$ (∇).

behaviour, we study the evolution of the tangent at the spiral centre ($p = \pi$). It is easier to display the results as the time T_δ taken to reach the angle θ. The results are shown in figure 4 for a range of choices in δ. The numerical results are displayed as a series of symbols placed at regular spacings in time. There is a clear indication of a linear relation between T_δ and θ. We have included the best straight line fit,

$$T_\delta = a(\delta) + b(\delta)\theta, \tag{3.5}$$

in the range $3 < \theta < 40$ for each choice of δ and they are displayed as straight lines. The fits are extremely accurate with a deviation less then 10^{-4}. Also noticeable is the

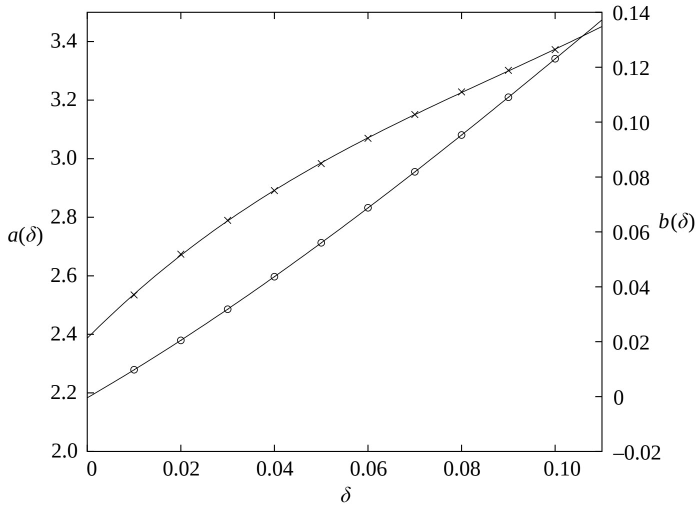

FIGURE 5. The intercept a (×) and slope b (○) as functions of δ. The solid curves are the least-squares fit to a cubic.

tendency for the angle to vary very rapidly in time for the smaller values of δ. This rapid variation of the angle means many turns of the spiral form very quickly.

The next stage in understanding the limit $\delta \to 0$ is to consider the dependency of the slope $b(\delta)$ and intercept $a(\delta)$ in the straight line fit (3.5). We show the intercept and slope in figure 5 for the range in δ given in figure 4. We also show the least-squares fit to a cubic polynomial:

$$a = 2.387 + 16.0\,\delta - 99.06\,\delta^2 + 379.6\,\delta^3, \tag{3.6a}$$

$$b = -0.00044 + 0.9856\,\delta + 3.231\,\delta^2 - 7.386\,\delta^3. \tag{3.6b}$$

The accuracy of these form fits is difficult to assess since they have been applied to data that is already the consequence of a straight line fit. The cubic fit to b appears reliable since the cubic term is small over the range in δ. Unfortunately, all terms are important for the cubic fit to a for values of $\delta \approx 0.1$. However, the visible comparison afforded in figure 5 is very good.

We can see that the constant 0.00044 in the cubic fit to b is much smaller in magnitude than the other three constants in the cubic. Further, the impression gained from the curves in figure 4 is that the slope is becoming horizontal as $\delta \to 0$. We assume, therefore, that the constant term in b should really be zero. If this is true, 3.5 should be written as

$$T_\delta = 2.387 + 16.0\,\delta + \ldots + (0.9856\,\delta + 3.231\,\delta + \ldots)\,\theta, \tag{3.7}$$

or more appropriately when δ is small

$$\tau = \frac{t - 2.387}{\delta} = 16.0 + 0.9856\,\theta. \tag{3.8}$$

This relation tells us clearly that to study the geometric similarity in the spirals (same θ), we must scale time to keep τ fixed. The origin of τ is $t = 2.387$ which is very close to estimates for the singularity time $t_s = 2.356$ by Krasny (1986a) and $t_s = 2.30$ by us.

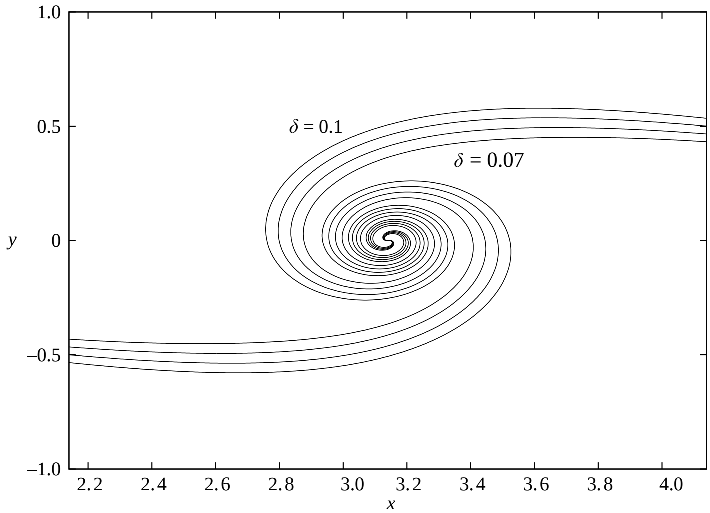

FIGURE 6. Vortex sheet locations with δ varying from 0.07 to 0.1 in steps of 0.01. Times are given in the text.

Unfortunately, (3.8) proves inadequate to determine the time at which spirals generated with δ in the range $(0.01, 0.1)$ will have the same angle θ at their centres because higher-order effects in δ as indicated in (3.6) are important. Instead, we use the form fit 3.5 to determine the time it will take for the spiral to reach an angle $\theta = 5\pi$ at its centre. For each choice of δ the time is different: in particular, for $\delta = 0.1$, $t = 5.3061$; for $\delta = 0.9$, $t = 5.0153$; for $\delta = 0.08$, $t = 4.7249$; for $\delta = 0.07$, $t = 4.4370$; for $\delta = 0.06$, $t = 3.8638$; for $\delta = 0.04$, $t = 3.5738$; and for $\delta = 0.02$, $t = 2.9956$. We display the results in figure 6 for a limited range in choices for δ simply to maintain clarity in the figure. Otherwise, the curves overlap and the pattern in the results is obscured.

The striking feature of the locations in figure 6 is that they appear to be evenly spaced. This suggests that the spiral should be scaled according to

$$\hat{x}(p) = \frac{x(p) - \pi}{\delta}, \quad \hat{y}(p) = \frac{y(p)}{\delta}. \tag{3.9}$$

We show the consequences of this rescaling in figure 7. The range in the scaled variables is such that the location of the sheet for $\delta = 0.1$ is unchanged. The collapse of the other curves onto a single spiral is almost perfect even for a much larger range in δ than shown in figure 6. Outside the spiral region, the curves do not overlap, but that is expected. Recall that Lagrangian points outside the spiral region converge linearly in δ when their locations are taken at the same time (see figure 3). This pattern will be broken when locations are chosen at different times, as is the case here. On the other hand, the lack of linear convergence for Lagrangian points inside the spiral region can now be understood as the consequence of choosing the locations at the same time instead of the scaled times used here. To pursue this point further, we show the y-coordinate of the vortex sheet as a function of the Lagrangian parameter p in figure 8 for the cases shown in figure 6. We have shifted the Lagrangian parameter so that it is centred at the spiral centre and we have zoomed onto the region of the spiral. The oscillatory pattern in the y-coordinate illustrates the turns of the spiral. The height of the oscillations reflect the scaling in δ given in (3.9), but what is also

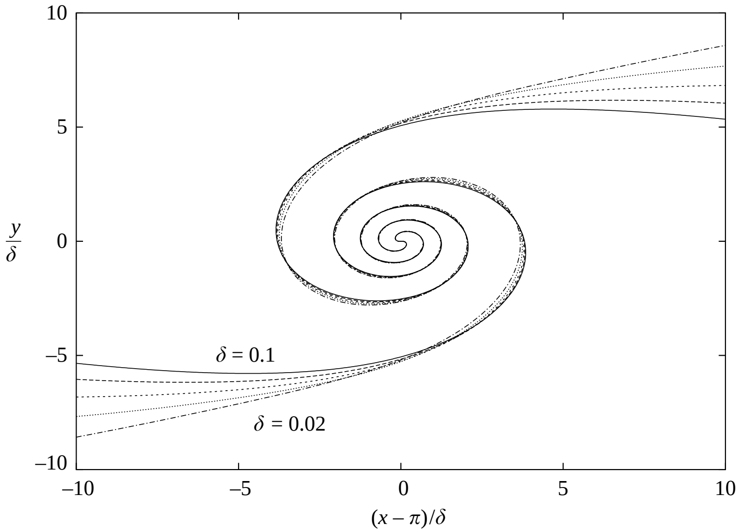

FIGURE 7. Rescaled vortex sheet locations for $\delta = 0.02, 0.04, 0.06, 0.08, 0.1$. Times are given in the text.

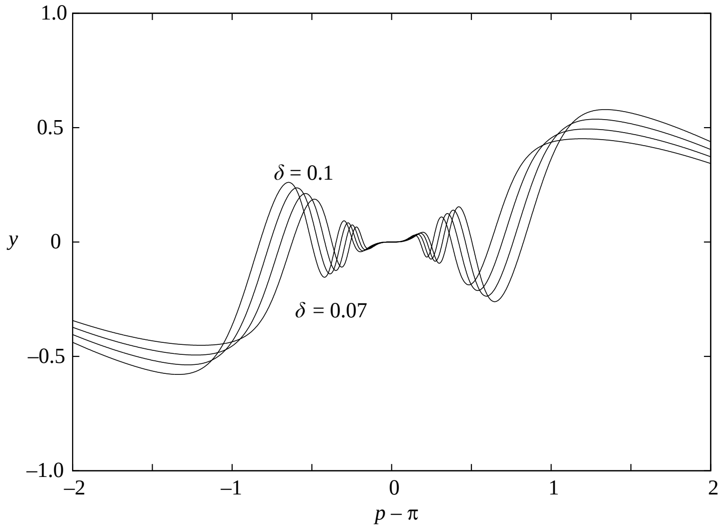

FIGURE 8. The y-coordinate of the vortex sheet as a function of the Lagrangian variable p for the same cases as in figure 6.

apparent is a uniform shift in the location of the peaks of the oscillation. Clearly, the Lagrangian variable should also be scaled,

$$\hat{p} = \frac{p - \pi}{\delta}. \tag{3.10}$$

The results of the scaling, shown in figure 9, are less impressive than the scaled spirals in figure 7. There remains a small non-uniform spacing between the cuves. There are several possible explanations for the spacing in the curves, the most obvious being that $p - \pi$ should be expressed in a power series similar to the one for the time variable (3.7) and that higher-order terms in δ are still important. Bearing in mind

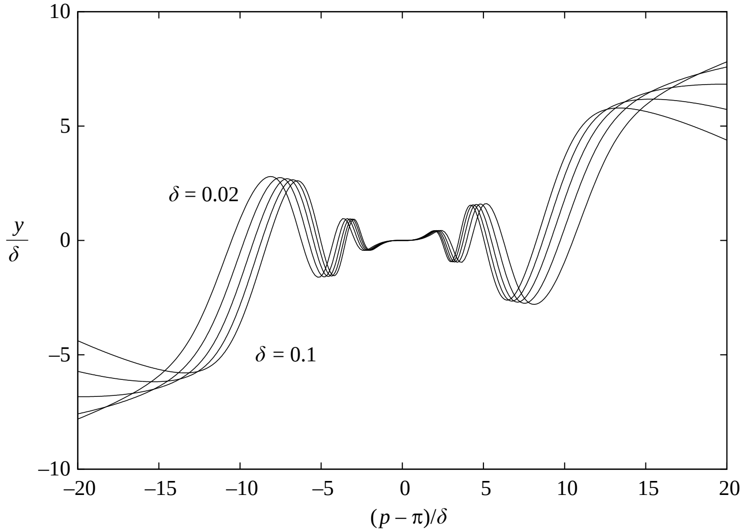

FIGURE 9. The scaled y-coordinate of the vortex sheet as a function of the scaled Lagrangian variable p for the same cases as in figure 7.

that gaps correspond to a difference of a few per cent in the original data, it seems reasonable to assume that the leading-order behaviour is given by (3.10).

In summary, the numerical evidence suggests that after t_s, the vortex sheet location behaves as

$$x(p,t) = X(p,t) + \delta X_1(p,t)\ldots, \tag{3.11a}$$

$$y(p,t) = Y(p,t) + \delta Y_1(p,t)\ldots, \tag{3.11b}$$

outside the spiral region, and as

$$x(p,t) = \pi + \delta F\left(\frac{p-\pi}{\delta}, \frac{t-t_c}{\delta}\right) + \ldots, \tag{3.12a}$$

$$y(p,t) = \delta G\left(\frac{p-\pi}{\delta}, \frac{t-t_c}{\delta}\right) + \ldots, \tag{3.12b}$$

inside the spiral region. Upon substitution of (3.12) into (2.11a) and (2.13), we obtain to leading order

$$\frac{\partial F}{\partial \tau}(\xi,\tau) = -\frac{1}{2\pi}\int_{-\infty}^{\infty} \frac{G(\xi,\tau)-G(\xi',\tau)}{(F(\xi,\tau)-F(\xi',\tau))^2+(G(\xi,\tau)-G(\xi',\tau))^2+1}\,\mathrm{d}\xi', \tag{3.13a}$$

$$\frac{\partial G}{\partial \tau}(\xi,\tau) = \frac{1}{2\pi}\int_{-\infty}^{\infty} \frac{F(\xi,\tau)-F(\xi',\tau)}{(F(\xi,\tau)-F(\xi',\tau))^2+(G(\xi,\tau)-G(\xi',\tau))^2+1}\,\mathrm{d}\xi'. \tag{3.13b}$$

where $\xi = (p-\pi)/\delta$ and $\tau = (t-t_s)/\delta$.

The first observation about (3.13) that should be made is that a solution exists globally in time because the equations are nothing more than the blob equations with $\delta = 1$. To construct a unique solution we anticipate the need for far-field conditions $|\xi| \to \infty$ and an initial condition at some time τ_i. Unfortunately, there are no obvious choices for these conditions. We will discuss the issues involved for each condition separately.

At first thought, it would seem that the natural initial condition for (3.13) would be at $\tau_i = 0$, when the singularity would form in the vortex sheet. However, the estimate

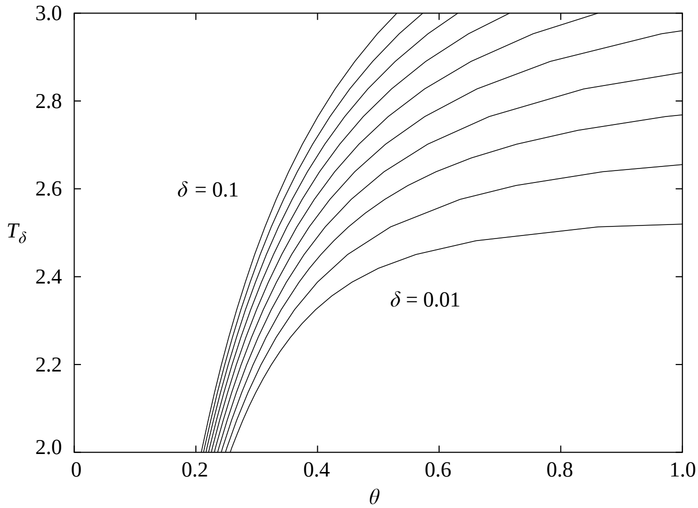

FIGURE 10. Time as a function of the sheet angle at the centre for δ ranging from 0.01 to 0.10 in steps of $\Delta\delta = 0.1$.

for t_s from the form fit (3.8) is slightly later than the estimate obtained by Krasny (1986*a*) ($t_s = 2.387$) or by Cowley *et al.* (1999) ($t_s = 2.30$). The question arises as to whether this occurs because there is another time scale close to the singularity formation during which the curve adjusts prior to settling into a late time pattern. Figure 10 shows the tangent angles at the centre as they evolve in time. The results are the same as in figure 4 except that curves are drawn in place of discrete values and the straight line fits have been removed.

The question that must be resolved is whether the curves indicate a dependency of the form $\theta = f(\tau)$. If this form is correct, then (3.13) will describe the transition of the curves from before the singularity time $\tau \ll 0$ through to the times where the relationship becomes linear. Consequently, the initial condition may be replaced by the requirement that solution to (3.13) as $\tau \to -\infty$ must match the behaviour of the solution to (2.16) using $\boldsymbol{K}_{BP}$ just before t_s as $\delta \to 0$.

By drawing a line at $\theta = 0.4$, it may be observed that the spacing grows slowly as $\delta \to 0$. Of course, this trend will simply reflect the effects of higher-order terms in δ. On the other hand, the trend may signal a difference scale in time, for example, $(t - t_s)/\sqrt{\delta}$. If this is true, there is another equation that describes the transition of the solution to the blob equations prior and after t_s. More detailed calculations will be required near t_s with much smaller values of δ to resolve these questions.

The impression from figure 7 is that the spiral which is a solution to (3.13) connects to the vortex sheet away from the spiral in a transition region. If P is a Lagrangian point in the transition or matching region to the right of π, then a solution to (3.13) must be found as $\delta \to 0$ such that $\delta\xi = P - \pi$. This means that in the limit $\xi = (P - \pi)/\delta \to \infty$, the solution must match the behaviour of the vortex sheet at p. The process is a familiar one associated with matched asymptotic expansions. Since the whole spiral appears to collapse to a single point in the limit as $\delta \to$, one possible matching condition is that the far-field behaviour of the spiral is the approach to some straight line.

The situation is made more complex because of the assumption of periodicity. The length scale implied by periodicity may force the transition region to occur close to the spiral, for instance, on the outer arms of the spiral. If periodicity is removed and the generation of the spiral occurs at a single location on the sheet, it is possible that the far-field behaviour of the spiral is simply to asymptote to a flat vortex sheet, an assumption made by Pullin (1981) in his study of the generalizations to the Kaden spirals. There is some indication in figure 7 that the transition region moves further away from the spiral centre as $\delta \to 0$, when the influence of periodicity diminishes. One way to settle the matter is to repeat our calculations without the assumption of periodicity and we are actively engaged in such calculations.

4. Conclusions

The evidence is strong that vortex blob methods provided a regularization of the vortex sheet for many choices of the smoothing function. If true, this would imply that the conditions assumed in the theory of Liu & Xin (1995) are not necessary, only sufficient. Our study of the convergence of the curves generated with a Krasny-type kernel ($\boldsymbol{K}_{BP}$) show two different regimes. In one, either prior to the singularity formation time or outside the spiral region, the convergence is clearly linear in δ. After the singularity time, the convergence in the spiral region is different: they scale according to (3.12). There remains some uncertainty about the nature of the curves near the singularity point at times very close to the singularity time as $\delta \to 0$.

The authors are deeply grateful for extremely valuable discussions with Dr Stephen Cowley and Professor Saleh Tanveer.

Appendix. The smoothing function for Krasny's periodic blobs

Suppose $\Phi(x, y)$ is a 2π-periodic function in x and that it has a discrete Fourier series with coefficients,

$$A_m = \int_0^{2\pi} \Phi(x, y)\, \mathrm{e}^{\mathrm{i}mx}\, \mathrm{d}x. \tag{A 1}$$

We seek $\phi(x, y)$ such that

$$\Phi(x, y) = \sum_{k=-\infty}^{\infty} \phi(x + 2k\pi, y). \tag{A 2}$$

Substitute (A 2) into (A 1),

$$\begin{aligned} A_m &= \int_0^{2\pi} \sum_{k=-\infty}^{\infty} \phi(x + 2k\pi, y)\, \mathrm{e}^{\mathrm{i}mx}\, \mathrm{d}x \\ &= \int_{-\infty}^{\infty} \phi(x, y)\, \mathrm{e}^{\mathrm{i}mx}\, \mathrm{d}x. \end{aligned} \tag{A 3}$$

Thus, the obvious choice for ϕ is that function with Fourier coefficients $a(m) = A_m$. In other words,

$$\phi(x, y) = \frac{1}{2\pi} \int_{-\infty}^{\infty} a(m)\, \mathrm{e}^{\mathrm{i}mx}\, \mathrm{d}m. \tag{A 4}$$

However, there are many functions whose periodic version is identically zero, for example, $f(x + \pi, y) - f(x - \pi, y)$. Any function with Fourier coefficients $a(m)$ that vanish when m is an integer can be added to ϕ, changing its periodic version.

For the Krasny periodic smoothing function (2.9b), the calculation of the Fourier coefficients A_m is simplified by introducing the change of integration variable $z = \exp(\mathrm{i}x)$.

$$A_m = -2\mathrm{i} \oint \frac{z^2 + 2Cz + 1}{[z^2 - 2(C + \delta^2)z + 1]^2} z^m \, \mathrm{d}z \tag{A 5}$$

where $C = \cosh(y)$ and the integration is around the unit circle in the anticlockwise direction. The integrand has a double pole inside the unit circle at

$$z = \mathrm{e}^{-L} \equiv C + \delta^2 - \sqrt{(C + \delta^2)^2 - 1}\,. \tag{A 6}$$

By the residue theorem,

$$A_m = \delta^2 \begin{cases} (m\alpha + \beta)\,\mathrm{e}^{-mL} & \text{for } m > 0, \\ (-m\alpha + \beta)\,\mathrm{e}^{mL} & \text{for } m < 0. \end{cases} \tag{A 7}$$

Finally, the basic smoothing function is determined by (A 4).

$$\begin{aligned} \phi(x, y) &= \frac{\delta^2}{2\pi} \int_0^\infty (m\alpha + \beta)\,\mathrm{e}^{-(L+\mathrm{i}x)m}\,\mathrm{d}m + \frac{\delta^2}{2\pi} \int_{-\infty}^0 (-m\alpha + \beta)\,\mathrm{e}^{(L-\mathrm{i}x)m}\,\mathrm{d}m \\ &= \frac{\delta^2}{\pi} \left[\frac{\alpha(L^2 - x^2)}{(L^2 + x^2)^2} + \frac{\beta L}{L^2 + x^2} \right]. \end{aligned} \tag{A 8a}$$

where

$$\alpha = \frac{\exp(-L)}{2\sinh^2(L)} \left[(\cosh(y) + \delta^2)(2\cosh(y) + \delta^2) - \delta^2 \sinh(L)\right], \tag{A 8b}$$

$$\beta = \frac{1}{2\sinh^3(L)} \left[\cosh(y)(\cosh(y) + \delta^2) + 1\right], \tag{A 8c}$$

$$\exp(-L) = \cosh(y) + \delta^2 - \sqrt{(\cosh(y) + \delta^2)^2 - 1}\,. \tag{A 8d}$$

We are unable to find a function $f(x, y)$, whose periodic version $f_p(x, y) = \sum_{k=-\infty}^{\infty} f(x + 2k\pi, y)$ is identically zero, that can be added to (A 8a) so that the result will satisfy the sufficient conditions for convergence to a weak limit.

REFERENCES

Baker, G. R. 1983 Generalized vortex methods for free-durface flows. In *Waves on Fluid Interfaces* (ed. R. E. Meyer). Academic.

Baker, G. R. & Shelley, M. J. 1990 On the connection between thin vortex layers and vortex sheets. *J. Fluid Mech.* **215**, 161–194.

Beale, J. T. & Majda, A. 1985 High order accurate vortex methods with explicit velocity kernels. *J. Comput. Phys.* **58**, 188–208.

Caflisch, R. E. & Orellana, O. F. 1989 Singular solutions and ill-posedness for the evolution of vortex sheets. *SIAM J. Math. Anal.* **20**, 293–307.

Chorin, A. & Bernard, P. 1973 Discretization of a vortex sheet, with an example of roll-up. *J. Comput. Phys.* **13**, 423–429.

Cowley, S. J., Baker, G. R. & Tanveer, S. 1999 On the formation of Moore curvature singularities in vortex sheets. *J. Fluid Mech.* **378**, 233–268.

Delort J.-M. 1991 Existence de nappes de tourbillon en dimension deux. *J. Am. Math. Soc.* **4**, 553–586.

Dhanak, M. R. 1994a On the equation of motion of a thin layer of uniform vorticity. *Stud. Appl. Maths* **92**, 115–125.

Dhanak, M. R. 1994b Equation of motion of a diffusing vortex sheet. *J. Fluid Mech.* **269**, 265–281.

Krasny, R. 1986*a* A study of singularity formation in a vortex sheet by the point vortex method. *J. Fluid Mech.* **167**, 65–93.

Krasny, R. 1986*b* Desingularization of periodic vortex sheet roll-up. *J. Comput. Phys.* **65**, 292–313.

Krasny, R. 1987 Computation of vortex sheet roll-up in the Trefftz plane. *J. Fluid Mech.* **184**, 123–155.

Kuwahara, K. & Takami, H. 1973 Numerical studies of two-dimensional vortex motion by a system of point vortices. *J. Phys. Soc. Japan* **34**, 247–253.

Liu, J.-G. & Xin, Z. 1995 Convergence of vortex methods for weak solutions to the 2D Euler equations with vortex sheet data. *Commun. Pure Appl. Maths* **48**, 611–628.

Majda, A. 1993 Remarks on weak solutions for vortex sheets with a distinguished sign. *Indiana Univ. Math. J.* **42**, 921–939.

Majda, A. & Bertozzi, A. 2002 *Vorticity and Incompressible Flow*. Cambridge University Press.

Moore, D. W. 1978 The equation of motion of a vortex layer of small thickness. *Stud. Appl. Maths* **58**, 119–140.

Pham, L. D. 2001 Regularization of periodic vortex sheets. PhD thesis, Ohio State University.

Pugh, D. A. 1989 Development of vortex sheets in Boussinesg flows – formation of singularities. PhD thesis, University of London.

Pullin, D. I. 1981 On a generalization of Kaden's problem. *J. Fluid Mech.* **104**, 45–53.

Saffman, P. G. 1992 *Vortex Dynamics*. Cambridge University Press.

Sidi, A. & Israeli, M. 1988 Quadrature methods for periodic singular and weakly singular Fredholm integral equations. *J. Sci. Comput.* **3**, 201–219.

Tryggvason, G., Dahm, W. J. & Sbeih, K. 1991 Fine-structure of vortex sheet rollup by viscous and inviscid simulation. *Trans. ASME* I: *J. Fuids Engng* **113**, 31–36.